Quantitative ^{89}Zr Immuno-PET for In Vivo Scouting of ^{90}Y-Labeled Monoclonal Antibodies in Xenograft-Bearing Nude Mice

Iris Verel, MS[1]; Gerard W.M. Visser, PhD[2]; Ronald Boellaard, PhD[3]; Otto C. Boerman, PhD[4]; Julliette van Eerd, BS[4]; Gordon B. Snow, MD, PhD[1]; Adriaan A. Lammertsma, PhD[3]; and Guus A.M.S van Dongen, PhD[1]

[1]Department of Otolaryngology/Head and Neck Surgery, VU University Medical Center, Amsterdam, The Netherlands; [2]Radionuclide Center, VU University, Amsterdam, The Netherlands; [3]PET Center, VU University Medical Center, Amsterdam, The Netherlands; and [4]Department of Nuclear Medicine, University Medical Center Nijmegen, Nijmegen, The Netherlands

Immuno-PET as a scouting procedure before radioimmunotherapy (RIT) aims at the confirmation of tumor targeting and the accurate estimation of radiation dose delivery to both tumor and normal tissues. Immuno-PET with ^{89}Zr-labeled monoclonal antibodies (mAbs) and ^{90}Y-mAb RIT might form such a valuable combination. In this study, the biodistribution of ^{89}Zr-labeled and ^{88}Y-labeled mAb (^{88}Y as substitute for ^{90}Y) was compared and the quantitative imaging performance of ^{89}Zr immuno-PET was evaluated. **Methods:** Chimeric mAb (cmAb) U36, directed against an antigen preferentially expressed in head and neck cancer, was labeled with ^{89}Zr using the bifunctional chelate *N*-succinyldesferrioxamine B (*N*-sucDf) and with ^{88}Y using the bifunctional chelate *p*-isothiocyanatobenzyl-1,4,7,10-tetraazacyclododecane-1,4,7,10-tetraacetic acid (*p*-SCN-Bz-DOTA). The radioimmunoconjugates were coinjected in xenograft-bearing nude mice, and biodistribution was determined at 3, 24, 48, 72, and 144 h after injection. ^{89}Zr was evaluated and compared with ^{18}F in phantom studies to determine linearity, resolution, and recovery coefficients, using a high-resolution research tomograph PET scanner. The potential of PET to quantify cmAb U36-*N*-sucDf-^{89}Zr was evaluated by relating image-derived tumor uptake data (noninvasive method) to ^{89}Zr uptake data derived from excised tumors (invasive method). **Results:** ^{89}Zr-*N*-sucDf-labeled and ^{88}Y-*p*-SCN-Bz-DOTA-labeled cmAb U36 showed a highly similar biodistribution, except for sternum and thighbone at later time points (72 and 144 h after injection). Small differences were found in kidney and liver. Imaging performance of ^{89}Zr approximates that of ^{18}F, whereas millimeter-sized (19–154 mg) tumors were visualized in xenograft-bearing mice after injection of cmAb U36-*N*-sucDf-^{89}Zr. After correction for partial-volume effects, an excellent correlation was found between image-derived ^{89}Zr tumor radioactivity and γ-counter ^{89}Zr values of excised tumors ($R^2 = 0.79$). **Conclusion:** The similar biodistribution and the favorable imaging characteristics make ^{89}Zr a promising candidate for use as a positron-emitting surrogate for ^{90}Y.

Key Words: ^{89}Zr; PET; monoclonal antibodies; xenograft-bearing nude mice; ^{90}Y

J Nucl Med 2003; 44:1663–1670

The use of radiolabeled monoclonal antibodies (mAbs) for the improvement of diagnosis and treatment of cancer continues to be an expanding area of research (*1*). The potential of this approach was demonstrated by, among others, ibritumomab tiuxetan (Zevalin; IDEC Pharmaceuticals), the first radioimmunotherapy (RIT) procedure that received approval by the U.S. Food and Drug Administration, in 2002 (*2*). Initially, the ibritumomab tiuxetan regimen (for treating non-Hodgkin's lymphoma) consisted of an imaging procedure for which the chelate-coupled mAb ibritumomab tiuxetan was labeled with ^{111}In, followed 1 wk later by an RIT procedure for which the same conjugate was labeled with ^{90}Y.

^{90}Y has a physical half-life of 64.1 h and emits high-energy β^--particles (100% β^-, $E_{\beta^-max} = 2.28$ MeV). The absence of γ-ray emission minimizes dose radiation burden for medical personnel and relatives and enables outpatient treatment. Whereas these characteristics make ^{90}Y attractive for therapy, the lack of associated photon emission does not allow external imaging of the in vivo distribution of the ^{90}Y-labeled antibody. Attempts have been made to use the ^{90}Y-associated bremsstrahlung for these purposes, but because of low bremsstrahlung photon counts, high amounts of ^{90}Y would be needed for quantitative imaging (*3,4*). For this reason, the method was judged to be of limited practical value for tracer imaging procedures. In practice, it is customary to use ^{111}In (half-life, 67.3 h; γ-rays, 171 and 245 keV) as a γ-emitting surrogate for tracing the biodistribution of ^{90}Y in RIT trials (*5–7*). For coupling to mAbs, the DOTA chelator is generally used because it binds these 3-valent radionuclides with a very high stability (*8*).

Performing radioimmunoscintigraphy as a tracer imaging procedure before RIT enables the confirmation of tumor targeting and the estimation of radiation dose delivery to both tumor and normal tissues. At least 3 requirements need to be met for optimal use of an imaging radioimmunoconjugate as a predictor of a therapeutic radioimmunoconjugate. First, imaging and RIT conjugates should have similar biodistribution. Second, radionuclides used for imaging and

Received Feb. 19, 2003; revision accepted May 22, 2003.

For correspondence or reprints contact: Guus A.M.S. van Dongen, PhD, Department of Otolaryngology/Head and Neck Surgery, VU University Medical Center, De Boelelaan 1117, P.O. Box 7057, 1007 MB Amsterdam, The Netherlands.

E-mail: gams.vandongen@vumc.nl

RIT should have similar physical half-lives, preferably matching the biologic half-lives of mAbs. Third, procedures for quantification of uptake and subsequent dose calculations should be reasonably accurate. With respect to the last requirement, mAb distribution has been estimated using planar gamma-camera imaging and SPECT. These procedures, however, have intrinsic limitations with respect to quantification, primarily on account of scatter and partial absorption of γ-photons in the tissue of a patient. Because of more accurate scatter and attenuation corrections, PET is better qualified for tracer quantification. Besides, PET provides superior spatial and temporal resolution for imaging.

In our search for candidate positron emitters for PET with mAbs (immuno-PET), we set up the production, purification, and antibody labeling of ^{89}Zr (half-life, 78.4 h) and ^{124}I (half-life, 100.3 h), as these tracers have physical half-lives that are compatible with the time needed for mAbs to achieve optimal tumor-to-nontumor ratios (typically 2–4 d for intact mAbs). Of these isotopes, ^{89}Zr (22.6% β^+, $E_{\beta+max}$ = 0.897 MeV; Fig. 1) can be obtained with high radionuclidic purity by a (p,n) reaction on ^{89}Y, an element that is an ideal target material because of its 100% natural abundance. Recently, stable coupling of ^{89}Zr to mAbs was accomplished using the chelate *N*-succinyldesferrioxamine B (*N*-sucDf) and new linker chemistry based on amide bond formation (*10*). In addition, preliminary in vitro data indicated residualization of the radionuclide after internalization of ^{89}Zr-labeled mAbs by tumor cells, a phenomenon also observed with ^{111}In and ^{90}Y but not with ^{131}I and ^{186}Re (I. Verel, et al., unpublished data).

Taking these considerations into account, it was postulated that immuno-PET with ^{89}Zr-labeled mAbs might be a useful scouting procedure for ^{90}Y-mAb RIT. In the present study, the potential of this approach was evaluated by studying the biodistribution of both conjugates on coinjection and by assessing the quantitative imaging performance of ^{89}Zr immuno-PET. For this purpose, nude mice with head-and-neck squamous cell carcinoma (HNSCC) xenografts were used as an in vivo model, chimeric mAb (cmAb) U36 was used for HNSCC targeting, a high-resolution research tomograph (HRRT) 3-dimensional (3D) PET scanner was used for imaging, and ^{88}Y (half-life, 107 d) was used instead of ^{90}Y to enable counting in a γ-counter. Biodistribution of cmAb U36-*N*-sucDf-^{89}Zr and cmAb U36-*p*-SCN-Bz-DOTA-^{88}Y conjugates was studied up to 6 d after injection. In addition, the potential of PET to quantify cmAb U36-*N*-sucDf-^{89}Zr was evaluated by relating image-derived tumor uptake data (noninvasive method) to ^{89}Zr data derived from excised tumors (invasive method).

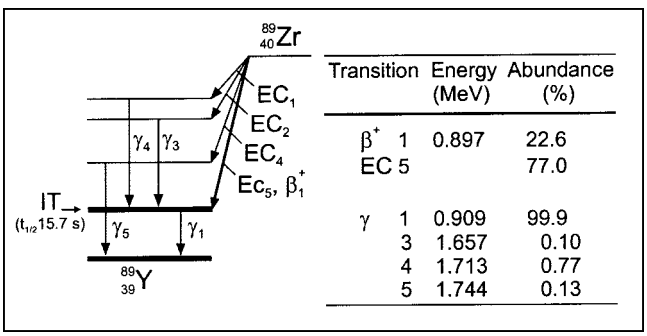

FIGURE 1. Simplified ^{89}Zr decay scheme (modified from ICRP publication (*9*)). Only transitions in excess of 0.1% abundance are shown. EC = electron capture; IT = isomeric transition; $t_{1/2}$ = half-life.

MATERIALS AND METHODS

mAb

Selection, production, and characterization of cmAb U36 have been described elsewhere (*11*).

Production and Isolation of ^{89}Zr

The improved procedure for ^{89}Zr production and isolation has been described recently in detail (*10*). Briefly, ^{89}Zr was produced via a (p,n) reaction on natural ^{89}Y by irradiating an ^{89}Y-layer on a copper support (14-MeV protons). The irradiated ^{89}Y-layer was dissolved in 2 mol/L HCl and, after addition of hydrogen peroxide, loaded onto a hydroxamate column. This column was washed with 2 mol/L HCl and sterile water to remove radionuclidic impurities and the bulk nonradioactive ^{89}Y and was eluted with 1 mol/L oxalic acid to obtain 99.99% pure ^{89}Zr.

Radiolabeling

Preparation of ^{89}Zr-Labeled cmAb U36. cmAb U36 was premodified with the chelate desferrioxamine B mesylate (Df) (Desferal; Novartis) via an amide linkage and labeled with ^{89}Zr according to recently described novel procedures (*10*). Df was succinylated (*N*-sucDf), temporarily filled with Fe(III), and coupled to mAbs by means of a tetrafluorophenol-*N*-sucDf-ester. On average, 1 Df-chelate per mAb molecule was conjugated. After premodification of the mAb, as well as after labeling of the premodified mAb with ^{89}Zr, the mAb solution was purified using a PD-10 column (Pharmacia Biotech), eluting with 5 mg/mL gentisic acid (pH 5). For biodistribution studies, cmAb U36-*N*-sucDf was labeled with 155 MBq ^{89}Zr and 2.2 mg mAb in a volume of 2.3 mL. For PET imaging studies, the reaction conditions were 3.6 mg premodified cmAb U36, 460 MBq ^{89}Zr, and a reaction volume of 6 mL.

Preparation of ^{88}Y-Labeled cmAb U36. cmAb U36 was conjugated with *p*-isothiocyanatobenzyl-1,4,7,10-tetraazacyclododecane-1,4,7,10-tetraacetic acid (*p*-SCN-Bz-DOTA; Macrocyclics), essentially as described by Hnatowich et al. (*12*). All steps were performed under strict metal-free conditions. A 50-fold molar excess of *p*-SCN-Bz-DOTA was added to cmAb U36 (10 mg/mL) in 0.1 mol/L $NaHCO_3$ buffer, pH 8.2, and incubated for 30 min at room temperature. Approximately 2 *p*-SCN-Bz-DOTA moieties were conjugated per mAb molecule. Nonconjugated chelator was removed by extensive dialysis against metal-free 0.25 mol/L NH_4OAc, pH 5.4. After dialysis, the chelated mAb was diluted in 0.25 mol/L NH_4OAc, pH 5.4, to a concentration of 1 mg/mL and stored at −20°C. cmAb U36-*p*-SCN-Bz-DOTA was labeled with ^{88}Y ($E_{main\ \gamma\text{-energies}}$ = 898 and 1,836 keV, 93.4% and 99.3% abundance, respectively) (74 MBq/mL; Isotope Products Europe Blaseg) by adding 5.6 MBq $^{88}YCl_3$ to 100 μg premodified cmAb U36 in 0.25 mol/L NH_4OAc, pH 5.4. After incubation for 60 min at 45°C, unbound ^{88}Y was removed using a PD-10 column eluted with phosphate-buffered saline, 0.5% bovine serum albumin.

Analyses

All conjugates were analyzed by instant thin-layer chromatography and high-performance liquid chromatography (for ^{89}Zr-conjugates) or fast protein liquid chromatography (for ^{88}Y-conjugates) for radiochemical purity, by sodium dodecylsulfate–polyacrylamide gel electrophoresis (SDS-PAGE) for integrity, and by a cell-binding assay for immunoreactivity.

High-performance liquid chromatography monitoring of the synthesis of cmAb U36-*N*-sucDf-^{89}Zr was performed as described previously (*10*). Fast protein liquid chromatography was performed with a Biosep Sec S3000 column (300 × 7.8 mm; Phenomenex) with a phosphate-buffered saline solution, pH 7.4, as eluent.

Instant thin-layer chromatography of radiolabeled mAbs was performed on silica gel–impregnated glass fiber sheets (Gelman Sciences Inc.). As the mobile phase, a citrate buffer concentration of 20 mmol/L, pH 5.0, was used for ^{89}Zr-labeled mAbs, and a concentration of 0.15 mol/L, pH 6.0, was used for ^{88}Y-labeled mAbs.

A germanium(lithium) detector coupled to a multichannel analyzer was used for absolute quantification of ^{89}Zr and for calibration of other detectors. Routine single-isotope radioactivity measurements of ^{88}Y and ^{89}Zr were performed with a dose calibrator or a γ-counter (LKB-Wallac, 1282 CompuGamma; Pharmacia). For quantification in a dose calibrator, the ^{54}Mn mode was used, multiplying the displayed amount of activity by a factor of 0.67 when measuring ^{89}Zr, and multiplying by a factor of 0.43 when measuring ^{88}Y. Quantification in a γ-counter was performed on the 909-keV γ-energy of ^{89}Zr and on the 898-keV γ-energy of ^{88}Y. For the dual-isotope counting of biodistribution studies, the 511-keV γ-energy of ^{89}Zr and the 1,837-keV γ-energy of ^{88}Y were used. Crossover corrections from one radionuclide into the alternate window were performed using a standard of each radionuclide.

The integrity of the radioimmunoconjugates was monitored by electrophoresis on a Phastgel System (Pharmacia Biotech) using preformed 7.5% SDS-PAGE gels under nonreducing conditions. Analysis and quantification of the radioactivity in the bands were performed with Phosphor Imager (B&L-Isogen Service Laboratory) screens and subsequent scanning by a Phosphor Imager.

In vitro binding characteristics of radiolabeled mAbs were determined in an immunoreactivity assay essentially described by Lindmo et al. (*13*), using UM-SCC-11B cells fixed in 0.1% glutaraldehyde.

Biodistribution

Nude mice bearing subcutaneously implanted human xenografts of the cell line HNX-OE were used. Female mice (athymic nu/nu, 21–31 g; Harlan CPB) were 10–14 wk old at the time of the experiments. All animal experiments were performed according to National Institutes of Health principles of laboratory animal care (*14*) and Dutch national law ("wet op de Dierproeven," Stb 1985, 336).

The mice were injected in the retroorbital plexus with a mixture of 0.37 MBq cmAb U36-*N*-sucDf-^{89}Zr, 0.13 MBq cmAb U36-*p*-SCN-Bz-DOTA-^{88}Y, and unlabeled cmAb U36 (total of 100 μg mAb). At indicated time points after injection, mice were anesthetized, bled, killed, and dissected. After blood, tumors (weight, 35–370 mg), normal tissues, and gastrointestinal contents had been weighed, the amount of radioactivity in each was measured in a γ-well counter. Radioactivity uptake was calculated as the percentage of the injected dose per gram of tissue (%ID/g). Differences in tissue uptake between coinjected conjugates were statistically analyzed for each time point with SPSS 10.0 software (SPSS Inc.) using the Student *t* test for paired data. Two-sided significance levels were calculated, and $P < 0.05$ was considered statistically significant.

PET Studies

PET Scanner. Measurements were performed using a prototype single-crystal-layer HRRT 3D PET scanner (CTI PET Systems) (*15*). The HRRT consists of 8 flat-panel detector heads, arranged in an octagon. The distance between 2 opposing heads is 46.9 cm. Each head contains 9 × 13 lutetium oxyorthosilicate crystal blocks of 7.5-mm thickness, which are cut into 8 × 8 crystals, resulting in 7,488 individual crystal elements per head and 59,904 crystals for the entire gantry.

Transmission scans for attenuation correction were routinely obtained with each scan in 2-dimensional (2D) mode (consisting of 52 scans with a total duration of 360 s) using a single point source of 740 MBq ^{137}Cs and an energy window of 550–800 keV. Emission data can be acquired in 3D mode only. For the present study, acquisition was performed with an energy window of 400–650 keV, and emission data were rebinned (compressed) online into 32-bit list mode using a span of 9 and a ring difference of 67. Random subtraction was applied online by a delayed window technique. The 32-bit list-mode file was subsequently converted into a single-frame histogram online.

For image reconstruction purposes, the transmission scan was first reconstructed and the resulting transmission image was scaled to correct for the difference in photon energy between emission (511 keV) and transmission (662 keV) counts using a histogram-based method (*15*). After attenuation correction and normalization (without correction for dead-time losses), the gaps in the resulting 3D emission sinogram were corrected by angular and transaxial interpolation. The fully corrected 3D emission scan was then Fourier rebinned into 207 image planes of 1.21 mm, which were subsequently reconstructed by 2D filtered backprojection with a Hanning 0.5 filter. The reconstructed volume consisted of 207 image planes of 256 × 256 voxels, with each voxel equaling 1.21 × 1.21 × 1.21 mm. For the present study, no scatter correction was applied because evaluation studies with the HRRT scanner showed that the scatter fraction was below 0.05 for small-animal scans and no accurate scatter-correction algorithm was available at the moment for HRRT scans (*15*).

Phantom Studies. Three basic phantoms were used. For linearity measurements, a phantom consisting of a cylinder (4.5 cm in diameter × 11.9 cm long) filled with 200 MBq ^{89}Zr was scanned for 30 min at several time points during the decay of ^{89}Zr. Two line sources were used for determination of spatial resolution, one filled with ^{89}Zr and the other with ^{18}F as a reference. The 2 sources were inserted in the central axis of a water-filled cylinder (20 cm in diameter × 20 cm long) and located transaxially, 5 cm off center. For determination of recovery coefficients, a Jaszczak phantom was used. This phantom consists of a water-filled cylinder, containing 6 spheres with inner diameters ranging from 4.4 to 28 mm (0.05 to 11.5 cm^3). The spheres were filled with either ^{89}Zr or ^{18}F and scanned for 30 min.

Animal Studies. Mice bearing HNX-OE xenografts were injected with 3.7 MBq cmAb U36-*N*-sucDf-^{89}Zr (100 μg), and up to 4 mice were scanned simultaneously. The total activity within the field of view of the scanner stayed well within the region of linearity. Before being scanned, the mice were anesthetized with

sodium pentobarbital (75 mg/kg, intraperitoneally) and positioned in the PET scanner. A transmission scan of 360 s was performed, followed by a 60-min emission scan. At 24 and 48 h after injection 2 mice were scanned, and at 72 h after injection 8 mice were scanned. The mice were killed immediately after scanning, and tumors (weight, 19–154 mg) were excised and counted with both a germanium(lithium) detector and a γ-counter.

PET Data Analysis

Phantom Studies. The calibration factor to convert region-of-interest (ROI) counts/pixel/s to Bq/mL was determined by drawing an ROI in the image of the scanned cylinder. For the determination of the counting rate linearity, the observed counts were subsequently converted with the aid of this calibration factor and plotted as a function of known radioactivity concentration.

Spatial resolution of ^{89}Zr, expressed as full width at half maximum (FWHM), was calculated by linear interpolation of horizontal and vertical line profiles, averaged over 5 adjacent image planes. For comparison, the same was performed for ^{18}F.

Hot-spot recovery coefficients (HSRCs) of ^{89}Zr were determined by drawing an ROI for each sphere of the Jaszczak phantom, using a 50% isocontour (ROI including pixels with ≥50% of the maximum pixel radioactivity concentration). Subsequently, the HSRC was calculated for each sphere by dividing the measured radioactivity concentration in the ROI ($A_{m,\ sphere}$) by the measured radioactivity concentration in the ROI of the largest sphere ($A_{m,\ largest\ sphere}$). The ROI areas derived from this experiment were compared with the true sphere sizes to assess the accuracy of size prediction using a 50% isocontour. For comparison, the same was performed for ^{18}F.

Animal Studies. For the quantification of radioactivity in millimeter-sized tumors, 3D volumes of interest (VOIs) were drawn semiautomatically using software kindly provided by J. Nuyts (Katholieke Universiteit Leuven). The radioactivity concentration in these VOIs was corrected for partial-volume effects starting from the following equation:

$$A_{u,\ tumor} = (HSRC \cdot A_{c,\ tumor}) + (CSRC \cdot A_{m,\ surroundings}), \qquad \text{Eq. 1}$$

where $A_{u,\ tumor}$ is the uncorrected radioactivity concentration in the tumor measured by PET, consisting of a tumor self-contribution and a near-surroundings spillover contribution. $A_{c,\ tumor}$ is the radioactivity concentration in the tumor after correction for partial-volume effects, $A_{m,\ surroundings}$ is the measured radioactivity concentration in the surrounding tissue near the tumor, and CSRC is the cold spot recovery coefficient.

$A_{u,\ tumor}$ was determined by drawing an 80% isocontour VOI around the tumor. HSRCs were determined by drawing 80% isocontour VOIs around each sphere of the Jaszczak phantom and were plotted as a function of VOI volume. The relationship between hot- and cold-spot measurements was taken as described by Geworski et al. (*16*):

$$CSRC = 1 - HSRC. \qquad \text{Eq. 2}$$

$A_{m,\ surroundings}$ was determined for each tumor by drawing 2 ROIs in the plane with the maximum pixel radioactivity concentration, together specifying a ring-shaped area around the tumor with a thickness of 1 pixel. The inner ROI (ROI_1) marked the boundary of the tumor and was established by decreasing the percentage of the isocontour until reaching the largest tumor ROI volume that did not include nearby radioactivity-containing organs. Subsequently, the second ROI (ROI_2) was drawn with 2 times the diameter of ROI_1 in the *x*- and *y*-directions. The radioactivity concentration in the ring-shaped area ($A_{m,\ surroundings}$) was determined according to the following equation:

$$A_{m,\ surroundings} = \frac{(N_2 - N_1)}{(V_2 - V_1)}, \qquad \text{Eq. 3}$$

where N_1 and V_1 are the radioactivity and volume of ROI_1, respectively, and N_2 and V_2 are those of ROI_2.

Rewriting Equation 1 and substituting Equations 2 and 3 give the following equation used in this study:

$$A_{c,\ tumor} = \frac{A_{u,\ tumor}}{HSRC} - \frac{(1-HSRC) \cdot (N_2 - N_1)}{HSRC \cdot (V_2 - V_1)}. \qquad \text{Eq. 4}$$

$A_{c,\ tumor}$ values (PET assessed) were plotted against the actual radioactivity levels in the excised tumors (ex vivo assessed), and regression analysis was performed with SPSS 10.0.

RESULTS

Radiolabeling

Labeling of cmAb U36-*N*-sucDf with ^{89}Zr resulted in an overall yield of 81% ± 6%, a radiochemical purity of 97.4% ± 0.9%, and 93% ± 2% immunoreactivity ($n = 2$). cmAb U36-*p*-SCN-Bz-DOTA was labeled with ^{88}Y with an overall yield of 97%, a radiochemical purity of 100%, and 96% immunoreactivity. Upon phosphor imager analysis of SDS PAGE gels, all 3 radioimmunoconjugates showed more than 92% of the activity in the 150-kDa IgG band. The specific activities of cmAb U36-*N*-sucDf-^{89}Zr for biodistribution and PET studies and of cmAb U36-*p*-SCN-Bz-DOTA-^{88}Y were 50, 109, and 46 MBq/mg, respectively.

Biodistribution Studies

For comparison of the biodistribution of ^{89}Zr-labeled and ^{88}Y-labeled mAb in tumor-bearing nude mice, cmAb U36-*N*-sucDf-^{89}Zr was coinjected with cmAb U36-*p*-SCN-Bz-DOTA-^{88}Y. At 3, 24, 48, 72, and 144 h after injection, the average uptake (%ID/g, mean ± SE) in tumor, blood, normal tissues, and gastrointestinal contents was determined (Fig. 2). In general, ^{89}Zr-labeled mAb and ^{88}Y-labeled mAb showed similar uptake in tumor, blood, and other organs at all time points. Tumor uptake increased over time, from 4.1 ± 0.3 %ID/g at 3 h to 25.7 ± 1.9 %ID/g at 144 h for the ^{89}Zr-labeled mAb and from 4.0 ± 0.3 %ID/g at 3 h to 25.9 ± 1.8 %ID/g at 144 h for the ^{88}Y-labeled mAb. Blood values decreased from 28.8 ± 0.8 %ID/g at 3 h to 6.9 ± 0.4 %ID/g at 144 h for the ^{89}Zr-labeled mAb and from 29.9 ± 0.9 %ID/g at 3 h to 7.9 ± 0.7 %ID/g at 144 h for the ^{88}Y-labeled mAb. Significant differences ($P < 0.01$) between ^{89}Zr-labeled mAb and ^{88}Y-labeled mAb were found at 72 and 144 h after injection in liver (6.9 ± 0.8 %ID/g vs. 6.2 ± 0.8 %ID/g and 7.7 ± 0.5 %ID/g vs. 6.0 ± 0.4 %ID/g, respectively), sternum (2.5 ± 0.1 %ID/g vs. 1.6 ± 0.03 %ID/g and 1.8 ± 0.2 %ID/g vs. 1.1 ± 0.1 %ID/g, respectively), and thighbone (2.5 ± 0.1 %ID/g vs. 1.3 ± 0.1 %ID/g and 3.5 ± 0.4 %ID/g vs. 1.1 ± 0.1 %ID/g, respec-

tively). For the kidney, a significant difference was found at all time points (from 7.3 ± 0.2 %ID/g vs. 6.5 ± 0.3 %ID/g at 3 h to 3.2 ± 0.2 %ID/g vs. 2.4 ± 0.2 %ID/g at 144 h).

PET Studies

Phantom Studies. ^{89}Zr phantom studies were performed to determine linearity, resolution, and recovery coefficients.

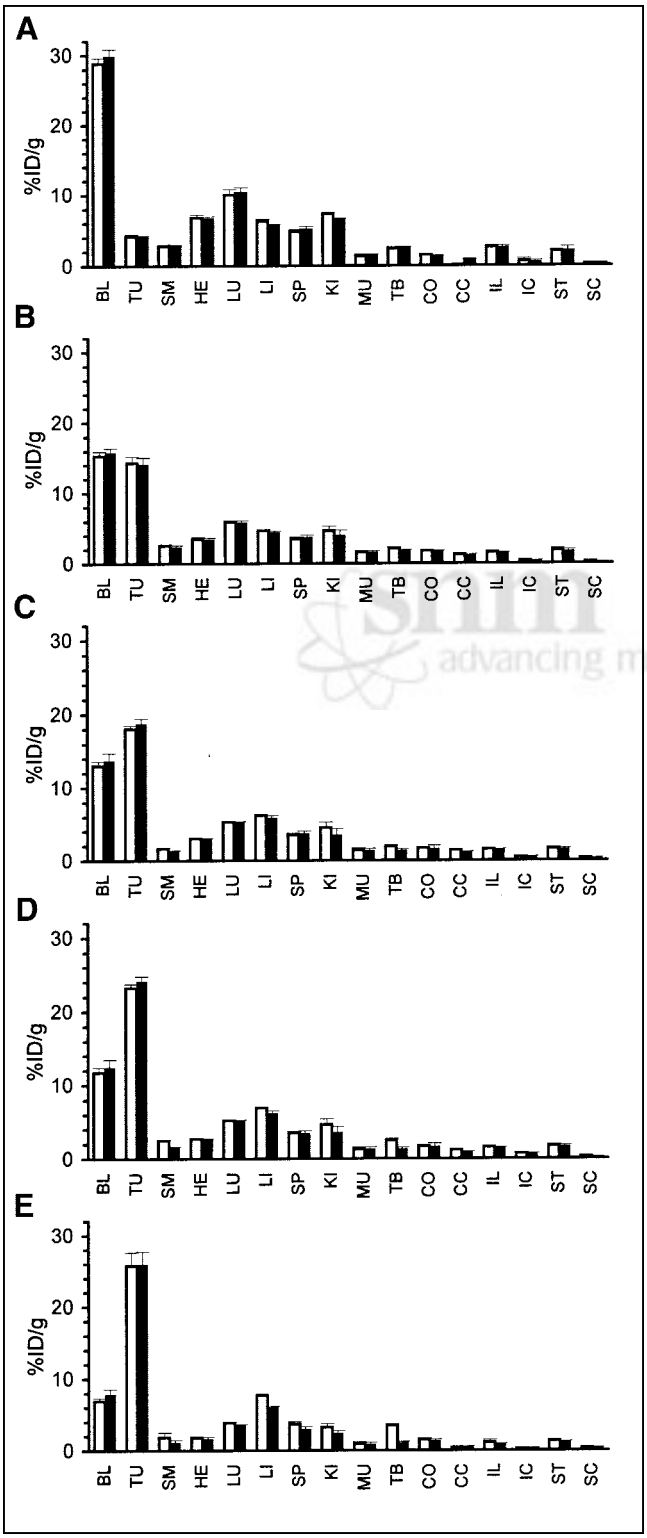

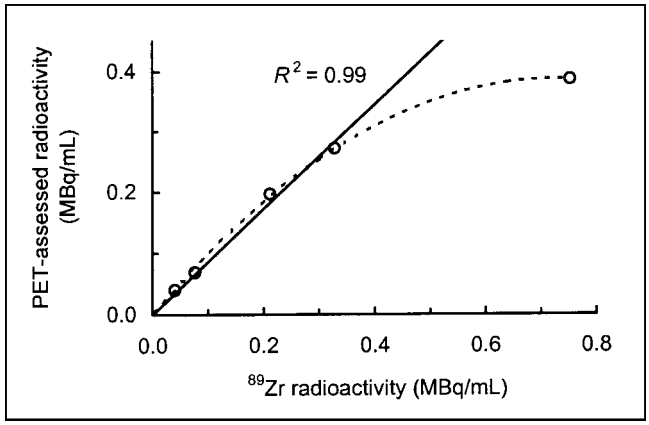

FIGURE 3. ^{89}Zr-counting-rate linearity determination with HRRT PET camera. Plot is of PET-assessed radioactivity in cylinder phantom versus radioactivity based on dose calibrator measurements. Note presence of linearity, except for highest radioactivity measurement.

Linearity (PET-assessed radioactivity concentration vs. the actual radioactivity concentration) was high (R^2 = 0.99) in the radioactivity range of 0.04–0.33 MBq ^{89}Zr per milliliter. At the highest radioactivity concentration measured, 0.75 MBq/mL, nonlinearity was observed (Fig. 3). Image resolution of ^{89}Zr, expressed as FWHM, was 4.0 mm (Fig. 4). Under the same conditions, FWHM for ^{18}F was 3.9 mm. HSRC (50% isocontour) for ^{89}Zr and ^{18}F as a function of sphere volume is shown in Figure 5A. In general, the ^{89}Zr-HSRC values were slightly lower than the ^{18}F-HSRC values. At 50% isocontour, the sphere areas were overestimated by a factor of 1.29 for ^{89}Zr and 1.07 for ^{18}F (Fig. 5B). The lower HSRC values and the higher overestimation of sphere areas of ^{89}Zr are most probably related to the higher positron energy of ^{89}Zr ($E_{\beta+max}$ = 0.897 MeV) in comparison with that of ^{18}F ($E_{\beta+max}$ = 0.634 MeV).

Animal Studies. Tumor imaging with ^{89}Zr-*N*-sucDf-labeled mAb was successful in 22 of 22 tumors (19–154 mg, 12 mice). Figure 6 shows a typical image of a xenograft-bearing nude mouse at 72 h after injection, with excellent visualization of tumors. The same studies were used to assess the potential of PET for quantification of tumor uptake. PET analysis, applying corrections for partial-volume effects according to Equation 4, gave tumor uptake values in close agreement (R^2 = 0.79, 24% ± 17% error)

FIGURE 2. Biodistribution of coinjected cmAb U36-*N*-sucDf-^{89}Zr (0.37 MBq, white bars) and cmAb U36-*p*-BSCN-Bz-DOTA-^{88}Y (0.13 MBq, black bars) in HNX-OE xenograft-bearing mice at 3 h (A), 24 h (B), 48 h (C), 72 h (D), and 144 h (E) after injection. At the indicated time points, 4 mice were bled, sacrificed, and dissected, and radioactivity levels (%ID/g ± SE) of blood, tumor, organs, and gastrointestinal contents were assessed. BL = blood; TU = tumor; SM = sternum; HE = heart; LU = lung; LI = liver; SP = spleen; KI = kidney; MU = muscle; TB = thighbone; CO = colon; CC = colon content; IL = ileum; IC = ileum content; ST = stomach; SC = stomach content.

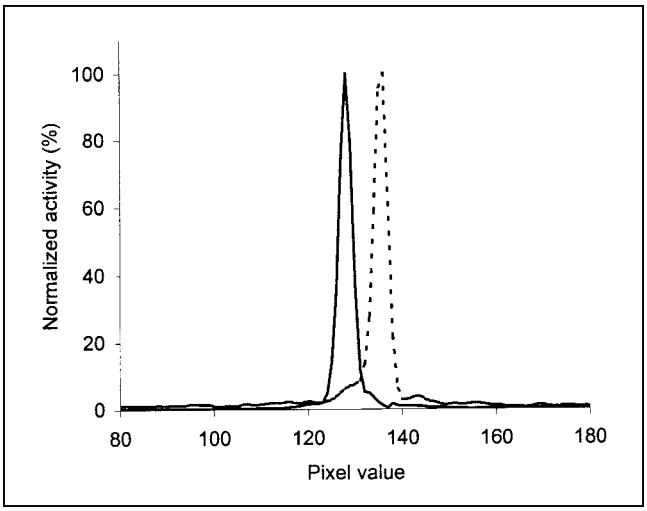

FIGURE 4. Spatial resolution determination for ^{89}Zr (dotted line) with HRRT PET camera. Line profile was drawn through image of line source containing ^{89}Zr. For comparison, line profile for ^{18}F (solid line) is also shown.

with ex vivo tumor uptake values (Fig. 7A). Figure 7B shows this correlation to be independent of the volume and the day of imaging. The result of quantification without correction for partial-volume effects is shown in Figure 7C and indicated that such correction is especially important for tumors with a small VOI.

DISCUSSION

Whereas ^{90}Y has attractive characteristics for therapy, imaging and the assessment of ^{90}Y biodistribution are complicated. The use of ^{111}In as an imaging analog for ^{90}Y has appeared to be suboptimal, because of the often-observed dissimilar biodistribution of these radionuclides (*5*). Besides this, imaging with ^{111}In uses a gamma camera, which has intrinsic limitations with respect to quantification. In theory, PET provides better possibilities for quantification of tracer uptake, but this technique is in its infancy with respect to the availability of suitable positron emitters, tracers, and quantification techniques (*17*).

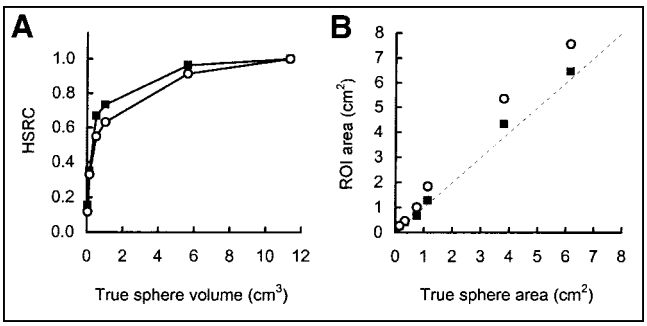

FIGURE 5. HSRCs (A) and sphere size estimations (B) for ^{89}Zr (○) with HRRT PET camera. For comparison, ^{18}F (■) data are also shown. For this purpose, 50% isocontour ROIs were drawn around spheres of Jaszczak phantom.

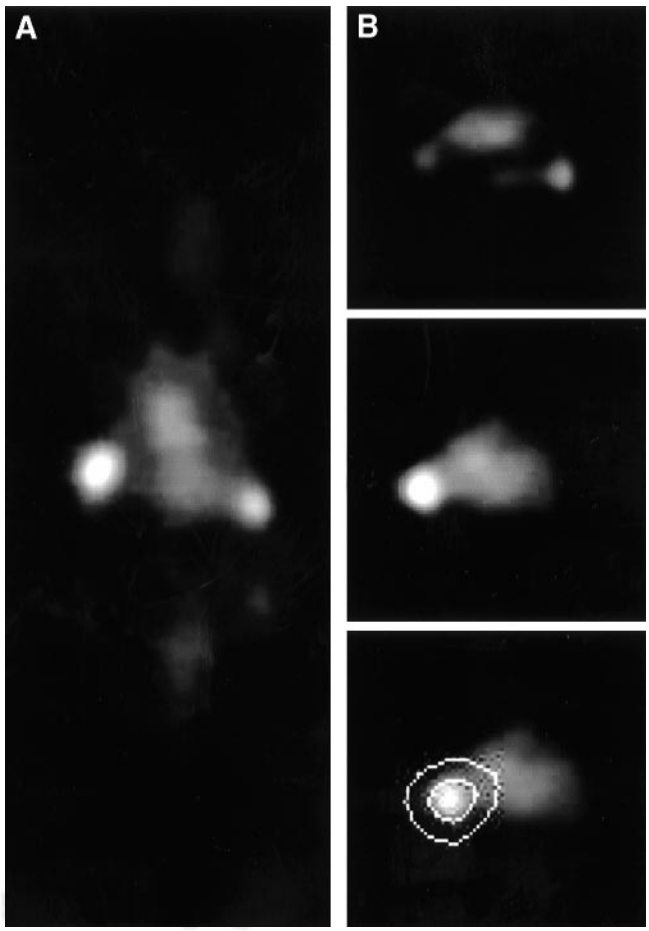

FIGURE 6. HRRT PET images of HNX-OE xenograft-bearing mouse injected with cmAb U36-*N*-sucDf-^{89}Zr (3.7 MBq) at 72 h after injection. Coronal image plane (A) in which both tumors (left, 124 mg; right, 26 mg) were visible was chosen. Transaxial image planes in which right tumor was optimally visible (B, top) or left tumor was optimally visible (B, middle and bottom) were chosen. Bottom panel of B illustrates approach to arrive at ring-shaped area used for surroundings determination.

Recently, we described the production of large batches of highly pure ^{89}Zr by a (p,n) reaction on natural yttrium (^{89}Y), and its stable coupling to mAbs (*10*). Because of the congruency in half-life of ^{89}Zr and ^{90}Y (78.4 vs. 64.1 h) and the fact that both radionuclides residualize on internalization, we postulated ^{89}Zr to be a suitable positron-emitting surrogate for ^{90}Y.

The present study was performed to examine the potential of immuno-PET with ^{89}Zr-labeled mAbs as a scouting procedure in combination with ^{90}Y-mAb RIT and to assess its quantitative imaging performance in a realistic setting, that is, small tumors in a region with low object-to-background ratio. As a first evaluation, the biodistribution of cmAb U36-^{89}Zr and cmAb U36-^{88}Y was compared using the *N*-sucDf chelate for coupling of ^{89}Zr and the commonly used chelate *p*-SCN-Bz-DOTA for coupling of ^{88}Y (instead of ^{90}Y). Notwithstanding different chelators, both radionuclides showed similar uptake levels in blood, tumor, and

most of the organs up to 144 h after injection. Only in kidney and, at the later time points (72 and 144 h after injection), in liver, sternum, and thighbone was a higher uptake of ^{89}Zr than of ^{88}Y observed. The difference in bone retention was in the same range as previously observed in biodistribution studies on ^{111}In- and ^{90}Y-labeled mAbs (*5*). The subtle divergence in biodistribution between ^{89}Zr and ^{88}Y is most probably due to the chemical differences between the radionuclides in combination with the chelators. With respect to the latter, investigations are ongoing to possibly find one chelate that binds both radionuclides with the same high stability.

As an alternative positron-emitting surrogate for ^{90}Y, ^{86}Y (33% β^+, $E_{\beta+max}$ = 1.2 MeV) has been receiving increasing attention (*18–24*). An advantage in the use of the same element would be that deconjugation should result in identical tissue distribution. With respect to ^{86}Y immuno-PET, the biodistribution of an ^{86}Y-labeled anti-Lewis Y mAb was recently compared with the biodistribution of the ^{111}In-labeled mAb, using 2-(*p*-SCN-Bz)-cyclohexyl-diethylenetriaminepentaacetic acid as the chelate (*23*). The uptake of ^{111}In and ^{86}Y was found to be similar in most tissues. In this study, no quantitative analysis with the authors' 2D PET system was performed, because of the difficulties met with from partial-volume effects when ^{86}Y is used to image small tumors. Moreover, the authors foresaw problems with ^{86}Y quantification when using 3D PET imaging equipment. These problems concern the subtraction of coincidences, which result from a 511-keV annihilation photon with a prompt γ-photon emitted by ^{86}Y. These so-called spurious true coincidences (not randoms) are accepted by the PET camera despite the fact that the 2 γ-photons have no angular correlation. As illustrated in phantom studies by Pentlow et al. (*22*), when using standard corrections on imaging of ^{86}Y with PET, such "spurious true coincidences" can introduce quantification artifacts, especially in regions of higher density. Solutions to these artifacts are under investigation (*22*).

Several aspects justify further development of ^{89}Zr-labeled radioimmunoconjugates in parallel with ^{86}Y-labeled conjugates. First, ^{89}Zr has no significant prompt γ-photons (Fig. 1), which can hamper quantification. As illustrated in this article, the quantitative imaging performance of ^{89}Zr was comparable to that of ^{18}F, and tumors as small as 19 mg were clearly visualized in xenograft-bearing nude mice after injection of ^{89}Zr-labeled cmAb U36. The potential of ^{89}Zr-PET for quantification was further illustrated by the good correlation between PET-assessed tumor uptake data and ex

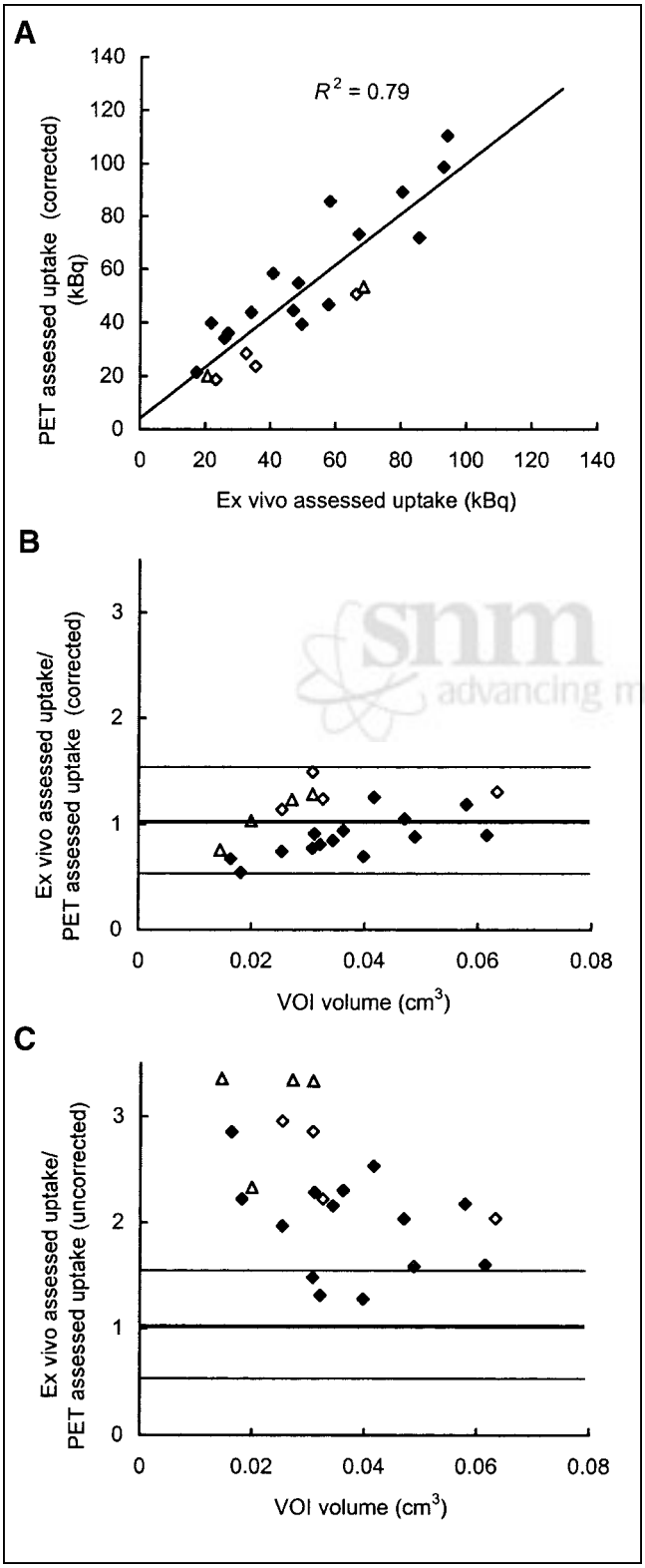

FIGURE 7. Correlation between PET-assessed tumor uptake and ex vivo–assessed tumor uptake. HNX-OE xenograft-bearing mice were injected with cmAb U36-*N*-sucDf-^{89}Zr (3.7 MBq) and scanned at 1 d (◇, n = 2), 2 d (△, n = 2), or 3 d (◆, n = 8) with HRRT PET camera. Immediately after being scanned, mice were dissected and radioactivity levels in tumors were determined with γ-counter. After reconstruction of images, VOIs were drawn over tumors and radioactivity amounts were calculated. (A) After correction for partial-volume effects, PET-assessed (image-derived) tumor radioactivity values were plotted as function of ex vivo–assessed (γ-counter–derived) tumor radioactivity values. Ratio of ex vivo–assessed and PET-assessed tumor radioactivity values, corrected (B) or not corrected (C) for partial-volume effects, was plotted as function of VOI.

vivo tumor uptake data ($R^2 = 0.79$). Second, the half-life of ^{89}Zr (78.4 h) better fits the time needed for intact mAbs to achieve optimal tumor-to-nontumor ratios (typically 48–96 h) than does the half-life of ^{86}Y (14.7 h). Also, the longer half-life of ^{89}Zr will evidently also have advantages for logistics related to labeling and transportation.

Because of the encouraging results herein, ^{89}Zr-labeled cmAb U36 IgG is currently being evaluated for its capacity to detect primary tumors and metastases in operable HNSCC patients. Moreover, the potential of ^{89}Zr immuno-PET for quantification will be further evaluated in that clinical study.

CONCLUSION

The biodistributions of cmAb U36-*N*-sucDf-^{89}Zr and cmAb U36-*p*-SCN-Bz-DOTA-^{88}Y matched well, except for sternum and thighbone at later time points (72 and 144 h after injection). Small differences were found in kidney and liver. The imaging performance of ^{89}Zr was comparable to that of ^{18}F, with a similar spatial resolution and HSRC. PET imaging with ^{89}Zr-labeled mAb did reveal millimeter-sized tumors in xenograft-bearing mice, with a good correlation between image-derived and ex vivo–determined tumor radioactivity. Thus, ^{89}Zr appears to be a promising candidate for use as a positron-emitting surrogate for ^{90}Y.

ACKNOWLEDGMENTS

The authors thank BV Cyclotron (VU University) for performing the irradiations; Jan H. Rector (Solid State Physics, VU University) for sputtering ^{89}Y on copper supports; Fred L. Buijs (Radionuclide Center, VU University) for analyzing the PET data; and Marijke Stigter, Maria J.W.D. Vosjan, and Liesbet Vervoort (VU University Medical Center) for contributing to the experiments.

REFERENCES

1. DeNardo SJ, Kroger LA, DeNardo GL. A new era for radiolabeled antibodies in cancer? *Curr Opin Immunol.* 1999;11:563–569.
2. Wagner HN, Wiseman GA, Marcus CS, et al. Administration guidelines for radioimmunotherapy of non-Hodgkin's lymphoma with ^{90}Y-labeled anti-CD20 monoclonal antibody. *J Nucl Med.* 2002;43:267–272.
3. Shen S, DeNardo GL, DeNardo SJ. Quantitative bremsstrahlung imaging of yttrium-90 using a Wiener filter. *Med Phys.* 1994;21:1409–1417.
4. Shen S, DeNardo GL, Yuan A, DeNardo DA, DeNardo SJ. Planar gamma camera imaging and quantitation of yttrium-90 bremsstrahlung. *J Nucl Med.* 1994;35: 1381–1389.
5. Carrasquillo JA, White JD, Paik CH, et al. Similarities and differences in ^{111}In- and ^{90}Y-labeled 1B4M-DTPA antiTac monoclonal antibody distribution. *J Nucl Med.* 1999;40:268–276.
6. Pai-Scherf LH, Carrasquillo JA, Paik C, et al. Imaging and phase I study of ^{111}In- and ^{90}Y-labeled anti-Lewis^{Y} monoclonal antibody B3. *Clin Cancer Res.* 2000;6: 1720–1730.
7. O'Donnell RT, DeNardo SJ, Yuan A, et al. Radioimmunotherapy with ^{111}In/^{90}Y-2IT-BAD-m170 for metastatic prostate cancer. *Clin Cancer Res.* 2001;7:1561–1568.
8. Meares CF, Moi MK, Diril H, et al. Macrocyclic chelates of radiometals for diagnosis and therapy. *Br J Cancer Suppl.* 1990;62:21–26.
9. Sowby FD, ed. *Radionuclide Transformations: Energy and Intensity of Emissions.* Oxford, England: Pergamon Press; 1983. ICRP publication 38, volumes 11–13.
10. Verel I, Visser GWM, Boellaard R, Stigter-van Walsum M, Snow GB, van Dongen GAMS. ^{89}Zr immuno-PET: comprehensive procedures for the production of ^{89}Zr-labeled monoclonal antibodies. *J Nucl Med.* 2003;44:1271–1281.
11. Schrijvers AHGJ, Quak JJ, Uyterlinde AM, et al. MAb U36, a novel monoclonal antibody successful in immunotargeting of squamous cell carcinoma of the head and neck. *Cancer Res.* 1993;53:4383–4390.
12. Hnatowich DJ, Childs RL, Lanteigne D, Najafi A. The preparation of DTPA-coupled antibodies radiolabeled with metallic radionuclides: an improved method. *J Immunol Methods.* 1983;65:147–157.
13. Lindmo T, Boven E, Luttita F, Fedorko J, Bunn PA Jr. Determination of the immunoreactive fraction of radiolabeled monoclonal antibodies by linear extrapolation to binding at infinite antigen excess. *J Immunol Methods.* 1984;72:77–89.
14. *Guide for the Care and Use of Laboratory Animals*. Washington, DC: Government Printing Office; 1985. NIH publication 86-23.
15. Boellaard R, Buijs F, de Jong HWAM, Lenox M, Gremillion T, Lammertsma AA. Characterization of a single LSO crystal layer high resolution research tomograph. *Phys Med Biol.* 2003;48:429–448.
16. Geworski L, Knoop BO, Levi de Cabrejas M, Knapp WH, Munz DL. Recovery correction for quantitation in emission tomography: a feasibility study. *Eur J Nucl Med.* 2000;27:161–169.
17. Eary JF. PET imaging for planning cancer therapy. *J Nucl Med.* 2001;42:770–771.
18. Herzog H, Rösch F, Stocklin G, Lueders C, Qaim SM, Feinendegen LE. Measurement of pharmacokinetics of yttrium-86 radiopharmaceuticals with PET and radiation dose calculation of analogous yttrium-90 radiotherapeutics. *J Nucl Med.* 1993;34:2222–2226.
19. Rösch F, Herzog H, Plag C, et al. Radiation doses of yttrium-90 citrate and yttrium-90 EDTMP as determined via analogous yttrium-86 complexes and positron emission tomography. *Eur J Nucl Med.* 1996;23:958–966.
20. Wester H-J, Brockmann J, Rösch F, et al. PET-pharmacokinetics of ^{18}F-octreotide: a comparison with ^{86}Ga-DFO- and ^{86}Y-DTPA-octreotide. *Nucl Med Biol.* 1997;24:275–286.
21. Rösch F, Herzog H, Stolz B, et al. Uptake kinetics of the somatostatin receptor ligand [^{86}Y]DOTA-DPhe^{1}-Tyr^{3}-octreotide ([^{86}Y]SMT487) using positron emission tomography in non-human primates and calculation of radiation doses of the ^{90}Y-labelled analogue. *Eur J Nucl Med.* 1999;26:358–366.
22. Pentlow KS, Finn RD, Larson SM, et al. Quantitative imaging of yttrium-86 with PET: the occurrence and correction of anomalous apparent activity in high density regions. *Clin Positron Imaging.* 2000;3:85–90.
23. Lövqvist A, Humm JL, Sheikh A, et al. PET imaging of ^{86}Y-labeled anti-Lewis Y monoclonal antibodies in a nude mouse model: comparison between ^{86}Y and ^{111}In radiolabels. *J Nucl Med.* 2001;42:1281–1287.
24. Garmestani K, Milenic DE, Plascjak PS, Brechbiel MW. A new and convenient method for purification of ^{86}Y using a Sr(II) selective resin and comparison of biodistribution of ^{86}Y and ^{111}In labeled Herceptin™. *Nucl Med Biol.* 2002;29: 599–606.